Nanosize Effects, Physicochemical Properties, And Catalytic Oxidation Pattern of the Redox-Precipitated MnCeO$_x$ System

Francesco Arena,*,†,‡ Giuseppe Trunfio,† Barbara Fazio,§ Jacopo Negro,† and Lorenzo Spadaro‡

Dipartimento di Chimica Industriale e Ingegneria dei Materiali, Università degli Studi di Messina, Salita Sperone 31 c.p. 29, I-98166 S. Agata (Messina), Italy, Istituto CNR-ITAE "Nicola Giordano", Salita S. Lucia 5, I-98126 S. Lucia (Messina), Italy, and Istituto di Processi Chimico-Fisici del CNR (CNR-IPCF) di Messina, Salita Sperone Contrada Papardo, I-98158 Faro Superiore (Messina), Italy

A series of *nanostructured* MnCeO$_x$ catalysts with superior textural and redox properties in comparison to coprecipitated systems was synthesized via the "redox-precipitation" route (*Chem. Mater.* **2007,** *19,* 2269). Characterization data prove that the redox-precipitated system consists of uniformly sized ($d \approx 20$ nm) spherical nanoparticles ensuring large surface area (120–260 m^2/g) and pore volume (0.5–0.6 cm^3/g), and a regular pore size distribution in a wide range of Mn/Ce ratios (1/3 to 3/1). The lack of long-range crystalline order and a homogeneous chemical composition signal that Mn and Ce oxides form composite nanodomains with a molecular dispersion of the active phase. Superior MnO$_x$ accessibility, strong MnO$_x$–CeO$_2$ interaction, and higher average oxidation number of both Mn and Ce ions strongly promote the reactive surface oxygen availability and the CO oxidation activity in the range of 323–423 K, also accounting for the better stability of the redox-precipitated system under reaction conditions.

Introduction

The urgent need to mitigate the harmful impact of anthropic activities on the environment is pressing the implementation of catalytic processes for effective waste detoxification. However, the extensive use of noble-metal catalysts represents to date a major drawback to the economical feasibility of present technologies. A major scientific concern, focused on low-cost catalyst formulations, allowed ascertaining the performance of MnCeO$_x$ systems for environmental applications, including wet air oxidation (CWAO) of toxic and biorefractory pollutants in wastewaters,[1–7] total oxidation of volatile organic compounds (VOCs),[8–14] and CO,[15,16] and selective reduction (SCR) of NO$_x$.[16,17]

Structure, dispersion, and chemical composition influence the catalytic pattern of the MnCeO$_x$ system having a superior activity generally associated with higher oxidation states (>+3) of Mn ions,[4,5,8,9,11,16–22] while stability and lifetime mostly rely on type and dispersion of MnO$_x$ phases and strength of the oxide–support interaction.[4,15–17] Then special synthesis routes[5–17,23–25] and adjustments in composition[4–6,19–26] were adopted for tuning the catalytic pattern of the title system. For instance, Qi and Yang reported that the sol–gel method promotes the NO$_x$ SCR activity,[17] while a modified coprecipitation route enhances the VOC combustion functionality of MnO$_x$–CeO$_2$ catalysts.[8] Further, Larachi et al. found an optimum Mn/Ce atomic ratio and a promoting effect of K on the phenol CWAO activity,[4,21] while Abecassis–Wolfovich et al. related a high chlorophenol CWAO performance of "nanocasted" MnCeO$_x$ catalysts to very large surface area and presence of a Mn$_5$O$_8$ phase.[6] Likewise, the redox-precipitation route enhances the CWAO activity of
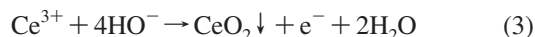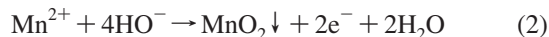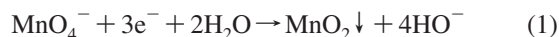
the MnCeO$_x$ system, owing to markedly better surface texture and active phase dispersion.[5,23–25]

Overall, such improved catalytic pattern depends on peculiar features of nanostructured materials since, besides a much higher surface area, a particle size smaller than 10 nm enables unprecedented electronic properties that strongly accelerate redox reactions.[6,15,23–29]

Therefore, this paper addresses the effects of preparation method and composition on the textural, redox, and catalytic properties of the MnCeO$_x$ system. Experimental data show that the redox-precipitation route leads to nanostructured systems with higher surface area, uniform pore size distribution, and molecular-like oxide dispersion, greatly promoting the surface oxygen mobility and the CO oxidation activity of MnCeO$_x$ catalysts.

Experimental Methods

Catalyst Preparation. MnCeO$_x$ catalysts with Mn/Ce atomic ratio (x/y) ranging between 1/3 and 3/1 (MxCy-R) were obtained via the redox-precipitation route,[5,23–25] consisting of titrating the KMnO$_4$ precursor ($\approx$10 g/L) with an aqueous solution of Ce^{3+}–Mn^{2+} salts at constant pH (8.0 ± 0.2)

$$MnO_4^- + 3e^- + 2H_2O \rightarrow MnO_2\downarrow + 4HO^- \qquad (1)$$

$$Mn^{2+} + 4HO^- \rightarrow MnO_2\downarrow + 2e^- + 2H_2O \qquad (2)$$

$$Ce^{3+} + 4HO^- \rightarrow CeO_2\downarrow + e^- + 2H_2O \qquad (3)$$

After titration, the solids were filtered, washed, and dried at 373 K (16 h) and further calcined (4 h) in air at 673 K (MxCy-R4). A coprecipitated MnCeO$_x$ sample (Mn/Ce, 1) calcined at 673 K (M1C1-P4) was taken as reference.[4,5,22–25] The list of samples with the relative notation and main physicochemical properties is given in Table 1.

Catalyst Characterization. Surface area (SA) and pore size distribution (PSD) were obtained from N$_2$ physisorption mea-

* Corresponding author, Francesco.Arena@unime.it.
† Dipartimento di Chimica Industriale e Ingegneria dei Materiali, Università degli Studi di Messina.
‡ Istituto CNR-ITAE "Nicola Giordano".
§ Istituto di Processi Chimico-Fisici del CNR (CNR-IPCF) di Messina.

TABLE 1: List of Catalysts and Main Physicochemical Properties

catalyst	preparation method	Mn/Ce^a des.	Mn/Ce^a exptl	Mn (wt %)	T_{calcd} (K)	SA (m^2/g)	PV (cm^3/g)	APD^b (nm)	Mn/Ce^c
M1C3-R	redox-precipitation	0.33	0.34	9.3		259	0.31	4.3	n.d.
M1C3-R4					673	168	0.28	5.1	0.58
M3C4-R	redox-precipitation	0.75	0.71	16.7		239	0.53	6.0	n.d.
M3C4-R4					673	169	0.47	7.2	1.00
M1C1-R	redox-precipitation	1.00	0.95	20.5		226	0.61	8.5	1.32
M1C1-R4					673	154	0.49	11.7	1.33
M3C2-R	redox-precipitation	1.50	1.44	26.6		208	0.62	9.7	n.d.
M3C2-R4					673	157	0.45	14.3	1.80
M2C1-R	redox-precipitation	2.00	2.12	32.7		206	0.59	10.4	n.d.
M2C1-R4					673	140	0.50	16.7	2.69
M3C1-R	redox-precipitation	3.00	2.76	36.8		185	0.52	12.4	n.d.
M3C1-R4					673	117	0.46	18.3	3.42
M1C1-P4	coprecipitation	1.00	1.00	21.2	673	101	0.24	9.4	0.40

^{a} Mn/Ce atomic ratio from design and XRF measurements, respectively. ^{b} Average pore diameter. ^{c} Mn/Ce atomic ratio from XPS measurements.

surements (77 K), using an ASAP 2010 (Micromeritics Instruments) static adsorption device. Isotherms were elaborated by the BET method for SA calculation, while micro- and mesopore distributions were obtained by Horvath−Kavazoe and BJH methods, respectively.

Scanning electron microscopy (SEM) analyses were performed using a field emission ZEISS Supra 25 microscope, working with an accelerating voltage of 5−10 kV, after Pt-sputtering of the samples.

Transmission electron microscopy (TEM) analysis was performed using a PHILIPS CM12 microscope on catalyst samples ultrasonically dispersed in isopropanol and deposited over a thin carbon film supported on a standard copper grid.

Micro-Raman spectra were taken at room temperature in back-scattering geometry, using a He−Ne laser excitation source (λ, 632.8 nm) focused onto the sample with a microscope (50×). An incident power of 0.5 mW was used to avoid thermal laser-induced effects. The signal was collected by the microscope, dispersed by a HR460 monochromator (Horiba-Jobin Yvon), and detected by a charge-coupled device array sensor (77 K) with a resolution of ca. 3 cm^{-1}.

X-ray photoelectron spectroscopy (XPS) data were obtained using a Physical Electronics GMBH PHI 5800-01 spectrometer operating with monochromatized Al Kα radiation with a power beam of 350 W. The pass energy for determination of the oxidation state and concentration of surface species were 11.0 and 58.0 eV, respectively. The BE regions of C 1s (280−300 eV), Mn 2p (635−680 eV) and Ce 3d (870−935 eV) were investigated, taking the C$_{1s}$ line (284.8 eV) of adventitious carbon as reference.

X-ray diffraction (XRD) analysis was performed by a Philips X-Pert diffractometer operating with Ni β-filtered Cu Kα radiation (40 kV; 30 mA) and a scan rate of 0.05 deg/min.

Reactive surface oxygen availability (RSOA) measurements in the range 293−423 K were carried out in continuous mode using a 10% CO/He mixture as carrier gas (30 stp mL min^{-1}). A catalyst sample ($\approx$30 mg) was loaded into a quartz microreactor, heated in a 10% O$_2$/He flow to 423 K (10 K/min), and then kept under isothermal conditions for 30 min. After the sample was allowed to cool to room temperature, the reactor was switched in the CO/He carrier and heated to 323, 373, or 423 K, manitaining isothermal conditions until the end of CO$_2$ formation (*reduction step*). Thereafter, oxygen treatment (*oxidation step*) in the 10% O$_2$/He flow at the same temperature was performed. Three reduction−oxidation cycles were run on each sample to address the catalyst stability.
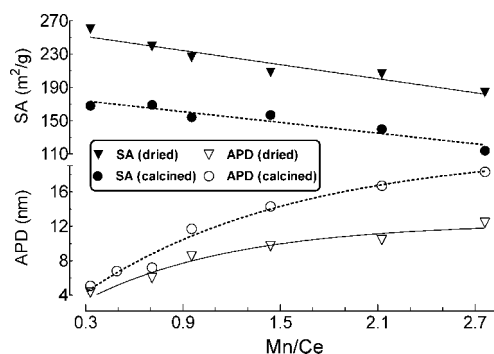

Figure 1. Influence of the Mn/Ce atomic ratio on surface area (SA) and average pore diameter (APD) of dried and calcined "redox-precipitated" catalysts.

Catalyst Testing. Kinetic measurements of CO oxidation in the range of 323−423 K were performed using a linear quartz microreactor (d_{int}, 4 mm) loaded with a catalyst sample (d_p, 0.03−0.05 mm) of 0.03−0.1 g diluted with 0.5 g of SiC (d_p, 0.3−0.5 mm). A CO/O$_2$/He mixture in the molar ratio 2/1/22 was fed at the rate of 0.1 stp L/min to ensure differential conversion levels (i.e., <8%). Before tests, the catalysts were pretreated at 423 K in an oxygen flow for 30 min. The temperature was controlled by a thermocouple inserted into catalyst bed, while the reaction stream was analyzed by gas chromatography. Reaction rate values were calculated from an average of three measurements after attainment of steady-state conditions ($\approx$1 h), while the absence of deactivation phenomena was assessed by performing two reaction cycles on each catalyst sample. The kinetic dependence on CO and O$_2$ pressure was probed varying p_{CO} and p_{O_2} in the ranges 0.04−0.1 (p_{O_2}, 0.04) and 0.04−0.2 (p_{CO}, 0.08), respectively.

Results and Discussion

(A) Effect of Synthesis and Composition on Texture and Structural Properties. Although we previously emphasized the potential of the redox-precipitation route in forwarding a fairly reproducible solid architecture,[23,24] the linear SA decay of dried and calcined systems and the concomitant growth of the average pore diameter (APD) with the Mn/Ce ratio (Figure 1) discloses a systematic composition effect on the surface texture of the redox-precipitated system.[25] Since the negligible effects of the "soft" drying treatment (*T*, 373 K), the negative influence of Mn loading on catalyst texture is clearly of chemical nature. In particular, a *cement*-like effect exerted by the MnO$_x$ phase[29]
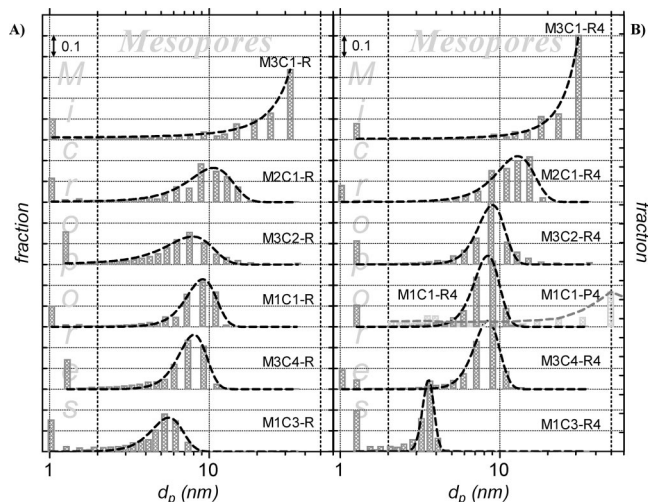
Figure 2. Pore size distribution of the dried (A) and calcined (B) redox-precipitated and coprecipitated catalysts.
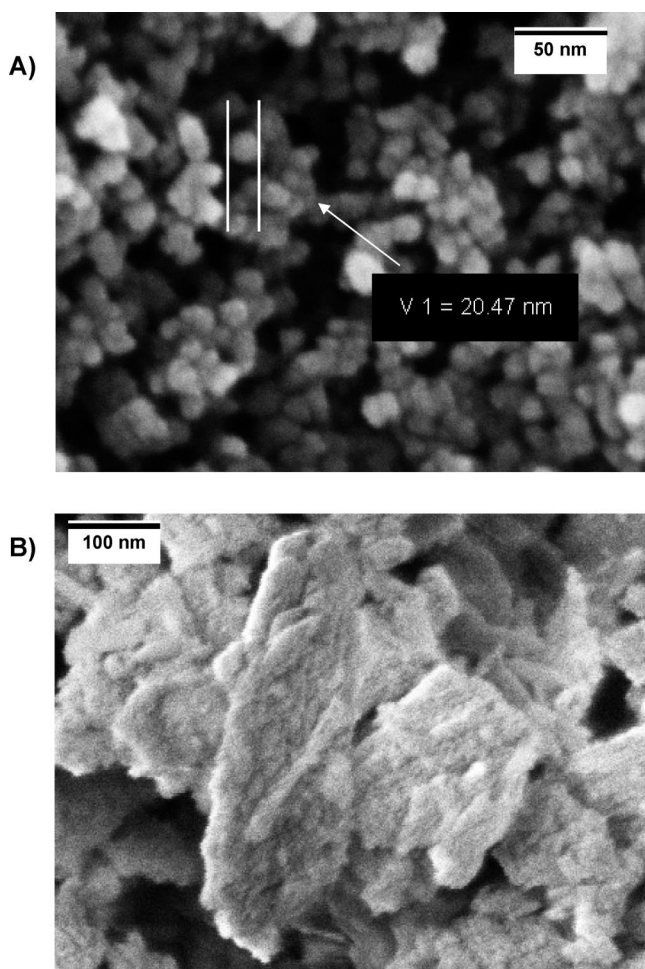

Figure 3. SEM photographs of M1C1-R4 (A) and M1C1-P4 (B) catalysts.

would promote the sticking of catalyst grains and the consequent closure of tinier pores (Figure 2). Apart from a minor contribution of micropores, the PSD of dried (Figure 2A) and calcined (Figure 2B) catalysts features a fairly narrow Gaussian shape, the center of which shifts from 4−5 to 10−11 nm upon the Mn/Ce ratio changes from 1/3 to 2/1. The composition effect also accounts for the apparently different PSD of the M3C1-R (Figure 2A) and M3C1-R4 (Figure 2B) samples, as a broadening
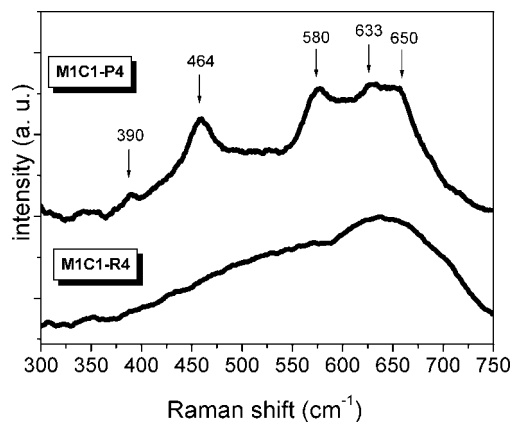

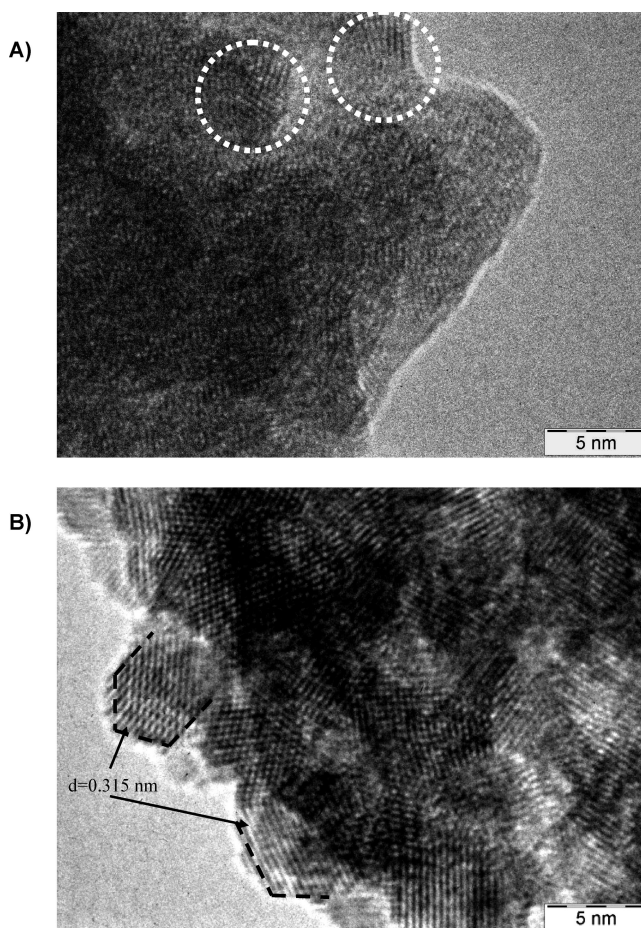**Figure 4.** Micro-Raman spectra of the M1C1-R4 and M1C1-P4 catalysts.

Figure 5. HRTEM photographs (×920000) of the M1C1-R4 (A) and M1C1-P4 (B) catalysts.

and upward shift displaces the descending branch of the Gaussian curve out of the mesopore range. Further, despite the ca. 30% decrease in SA due to surface dehydroxylation,[23] slight changes in PSD and pore volume (0.5−0.6 cm^3/g) confirm the minor influence of the calcination treatment on the texture of the redox-precipitated system.[23,25] All these features depend upon the straight formation of oxide phases in the redox-precipitation process and the consequent lack of solid-state transformations in the calcination step.[18,23,25] Lower SA, smaller PV, and flat PSD of the M1C1-P4 sample mirror instead a poor control of the coprecipitation technique on (i) composition−precursor (Ce^{4+}−Ce^{3+}, nitrates−chlorides) effects,[4−8,10−24] (ii) nucleation-

Nanostructured MnCeO$_x$ Catalysts

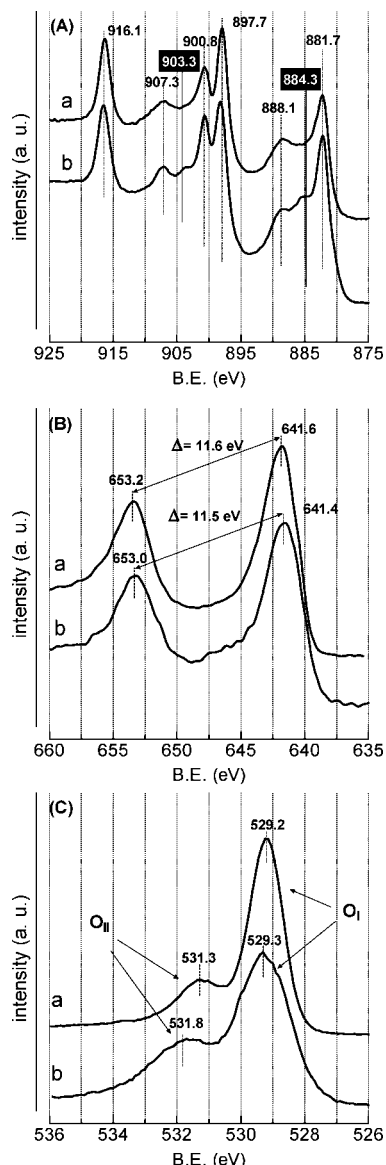*J. Phys. Chem. C, Vol. 113, No. 7, 2009* **2825**

Figure 6. XPS of the M1C1-R4 (a) and M1C1-P4 (b) catalysts: Ce 3d (A), Mn 2p (B), and O 1s (C) core level spectra.

TABLE 2: Summary of the XPS Data of the Calcined M1C1-R4 and M1C1-P4 Catalysts

	atomic abundance (%)[b]			Ce^{4+} u''' peak area (%)[a]	normalized surface composition
catalysts	Mn	Ce	O		
M1C1-R4	20.7	15.6	63.7	11.5	Mn$_{0.57}$Ce$_{0.43}$O$_{1.79}$
M1C1-P4	10.2	25.7	64.0	9.0	Mn$_{0.29}$Ce$_{0.71}$O$_{1.76}$

[a] Percentage peak area of the 916.1 eV transition of Ce 3d.
[b] Evaluated from the atomic abundance of Ce, Mn, and O.

growth processes,[18] and (iii) precursor-decomposition and phase-reconstruction phenomena during calcination.[4−14,16−22,25,28]

The above textural properties mirror a different catalyst morphology, according to SEM images of the M1C1-R4 (Figure 3A) and M1C1-P4 (Figure 3B) catalysts. The former sample consists of agglomerates of regularly sized (≈20 nm) spherical grains forming a spongelike structure with a fairly uniform porous network (Figure 2B), while the aggregation of stepped and irregular particles, sized from tens to hundreds nanometers (Figure 3B), explains the very inhomogeneous interparticle porosity of the coprecipitated system (Figure 2B).
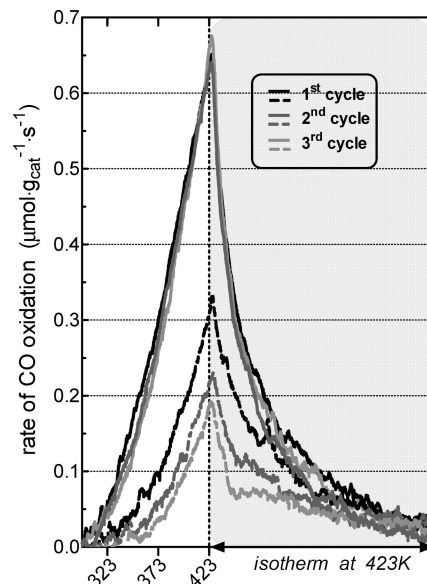

Figure 7. CO oxidation rate in absence of gas-phase oxygen between 293 and 423 K and in isotherm at 423 K of the M1C1-R4 (solid lines) and M1C1-P4 (dotted lines) catalysts.

These morphological features depend in turn upon a different structural pattern that was probed by micro-Raman (Figure 4) and HRTEM (Figure 5) analyses of the M1C1-R4 and M1C1-P4 catalysts. The Raman spectrum of the redox-precipitated system shows a featureless pattern denoting the lack of any long-range crystalline order, according to the HRTEM image (Figure 5A) displaying a prevalently amorphous background embedding few nanosized (<5 nm) crystalline nuclei with fringes of ca. 0.31 nm *d*-spacing of the ⟨111⟩ planes of cerianite.[23,24,28] This mostly amorphous pattern clearly leads to arguments against the formation of a classical crystalline oxide solid solution. A main peak at 462−464 cm^{-1}, due to the triply degenerate F$_{2g}$ active mode of the fluorite-type ceria lattice,[23,28,29] dominates instead the Raman pattern of the M1C1-P4 sample, in agreement with the massive presence of truncated-octahedral ceria domains (Figure 5B) with *d*-spacing of 0.31 and 0.27 nm, typical of the ⟨111⟩ and ⟨200⟩ crystal planes.[28] Although no additional crystalline phases are visible, the Raman spectrum displays some other peaks attributable to various MnO$_x$ crystalline species. The peak at ca. 390 cm^{-1} is due to the Mn−O bending, while the Mn−O stretching modes in the range of 500−700 cm^{-1} mask the weak component at ca. 590 cm^{-1} due to the nondegenerate Raman LO mode of ceria lattice.[23,29] The peak at 580 cm^{-1} and the broad "hill" in the range of 500−520 cm^{-1} are due to MnO$_2$,[30] while lines at 633 and 650 cm^{-1} monitor the presence of Mn$_2$O$_3$ and Mn$_3$O$_4$ phases, respectively.[31,32] Although reductive decomposition processes, due to laser-heating, allow the latter species to generally occur in Raman spectra of MnO$_2$,[30−32] the weak laser power (≈0.5 mW) used in this case substantiates the existence of various Mn oxides in the M1C1-P4 sample.[4−6,15,18−23,27] Indeed, earlier Raman analyses revealed the same crystalline CeO$_2$ and Mn$_2$O$_3$ species in both M1C1-R4 and M1C1-P4 catalysts as consequence of the sample-overheating phenomenon.[23]

(B) Surface Chemical Properties. The different structural pattern induced by the synthesis route has a strong influence also on the oxide dispersion,[23,24] according to the XPS values of the Mn/Ce atomic ratio of the various catalysts (Table 1). Although it could be argued that the photoelectron sampling depth compares with the size of oxide nanodomains of the redox-precipitated system, being such data no representative of

TABLE 3: Reactive Surface Oxygen Availability (RSOA) of the M1C1-R4 and M1C1-P4 Catalysts in the Range of 323−423 K

	1st cycle $(\mu mol_{O_2} \cdot g_{cat}^{-1})/(\mu mol_{O_2} \cdot m_{cat}^{-2})$			2nd cycle $(\mu mol_{O_2} \cdot g_{cat}^{-1})/(\mu mol_{O_2} \cdot m_{cat}^{-2})$			3rd cycle $(\mu mol_{O_2} \cdot g_{cat}^{-1})/(\mu mol_{O_2} \cdot m_{cat}^{-2})$		
catalyst	RSOA$_{323}$	RSOA$_{373}$	RSOA$_{423}$	RSOA$_{323}$	RSOA$_{373}$	RSOA$_{423}$	RSOA$_{323}$	RSOA$_{373}$	RSOA$_{423}$
M1C1-R4	4/0.03	48/0.31	198/1.29	4/0.03	45/0.29	175/1.13	5/0.03	49/0.32	186/1.21
M1C1-P4	0.5/0.005	10/0.01	104/1.03	0/0	7/0.07	68/0.67	0/0	5/0.05	56/0.55

an "usual" surface composition, yet those figures definitely point out a 2-fold concentration of manganese atoms in the outermost layers of M1C1-R4 system in comparison to the M1C1 P4 one.[19,29] The surface Mn depletion, usually found for coprecipitated MnCeO$_x$ systems,[4,19,23−25,29,37] discloses that such a higher active phase availability is a fundamental characteristic of the disclosed synthesis route irrespective of the Mn loading. Namely, a Mn/Ce XPS ratio slightly larger than bulk (Table 1) and the aforesaid lack of crystalline order substantiate the fact that the redox-precipitation route favors the sticking of Mn and Ce oxides at a quasi-molecular level.[23−25] Analogous Mn/Ce values of the M1C1-R and M1C1-R4 samples (Table 1) substantiate both the basic role of the synthesis route and the lack of significant structural changes in the calcination step.[23−25] At variance, the surface Ce enrichment of coprecipitated systems signals the tendency of MnO$_x$ precursors to segregate during precipitation and calcinations, leading to bulky crystalline species.[18−25,27,29]

(C) Surface and Redox Properties. Structure and dispersion affect the chemical state of Mn and Ce atoms, according to the Ce 3d (A), Mn 2p (B) and O 1s (C) spectra (Figure 6) and the main XPS data of the M1C1-R4 and M1C1-P4 catalysts in Table 2. The Ce 3d spectrum of the M1C1-R4 displays the six components (881.7−888.1; 897.7−900.8; 907.3−916.1 eV) of Ce^{4+}, while four additional transition states at 880.1, 884.3, 898.4, and 903.3 eV point out a detectable concentration of Ce^{3+} onto the M1C1-P4 system.[26,33−39] A larger relative area of the u''' component at 916.1 eV (Table 2), a measure of the amount of Ce^{4+},[19,29,33−37] confirms indeed the higher oxidation state of Ce while, according to the XPS atomic composition (Table 2), upward BE shift and larger Mn 2p$^{1/2}$−2p$^{3/2}$ spin−orbit split (Figure 6B) indicate a higher average oxidation number (AON)

also of manganese ions in the M1C1-R4 sample.[40−42] Minor AON of Ce and Mn ions in the M1C1-P4 sample rely on the precipitation of Ce^{3+} and Mn^{2+} salts and poor dispersion of oxides precursors, hindering an effective oxidation in the bulk further to calcination.[19,29,37] While, oxidizing strength of the KMnO$_4$ precursor and larger surface exposure concur to determine superior oxidation states in the redox-precipitated system. However, the O1s spectra (Figure 6C) display only minor effects of the preparation method on type and population of oxygen species. Namely, two components at 529.2−529.3 and 531.3−531.8 eV in the spectra of both systems arise from lattice ions (O$_I$) and surface oxygen species (O$_{II}$), respectively.[6,19,25,27,36,37] Though no attempt to relate the BE shift to Ce^{3+}/Ce^{4+} nor to Mn is made, the sharper profile of the O$_I$ peak well matches the higher chemical homogeneity of the redox-precipitated system. While, the origin of the O$_{II}$ component is controversial as it was attributed to hydroxyl-carbonate groups (531−532 eV), oxide defects (529−530 eV), adsorbed oxygen (531−532 eV) or water molecules (533−534 eV).[6,19,20,27,37] Since it is somewhat related to *oxygen vacancies* onto ceria lattice,[38,40−43] the prevailing exposure of ceria and its defective character could explain higher relative intensity and upward shift of this transition on the M1C1−P4 catalyst (Figure 6C).

Despite minor differences in the oxygen availability (Table 2), the XPS data signal a strong Mn enrichment in the surface and subsurface layers of the catalyst particles that well accounts for the easier reduction of the redox-precipitated system.[5,23−25] Indeed, molecular-like dispersion, higher AON of Mn and Ce
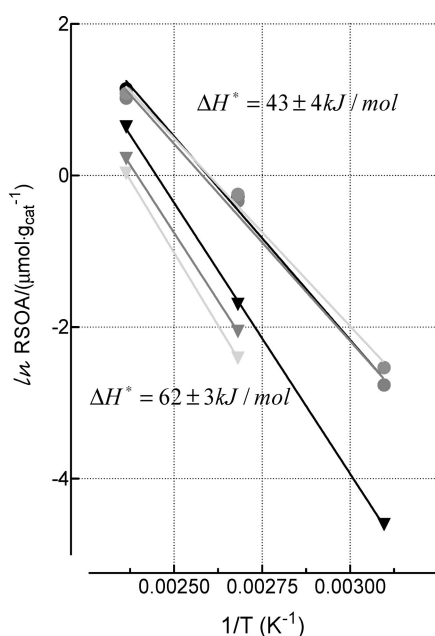

Figure 8. Arrhenius plot of reactive surface oxygen availability (RSOA) data of the M1C1-R4 and M1C1-P4 catalysts in the range of 323−423 K (see Table 3).
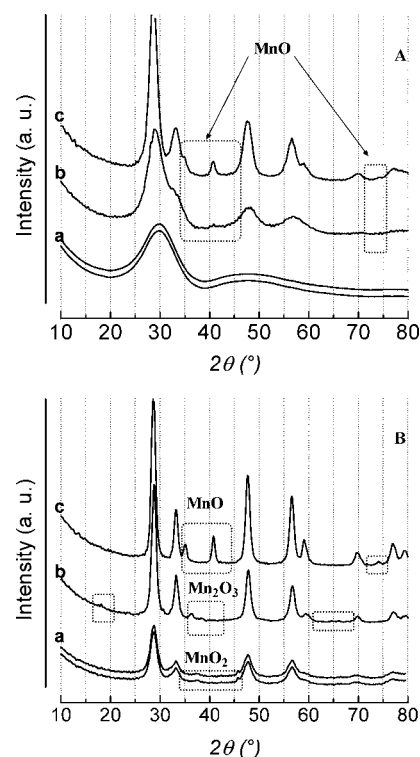

Figure 9. XRD patterns of the M1C1-R4 (A) and M1C1-P4 (B) catalysts reduced at 423 K (a); 585 K (b), and 720 K (c). The diffractograms of "untreated" samples (gray lines) are shown for reference.
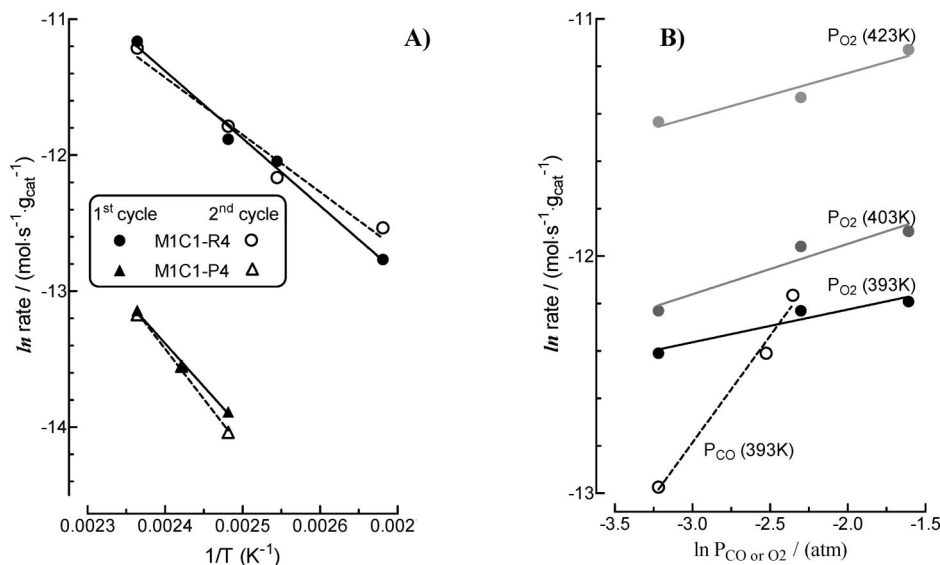
Nanostructured MnCeO$_x$ Catalysts

J. Phys. Chem. C, Vol. 113, No. 7, 2009 **2827**

Figure 10. (A) Arrhenius plot (373−423 K) of CO oxidation on M1C1-R4 and M1C1-P4 catalysts. (B) Dependence of reaction rate on CO and O$_2$ partial pressure at various temperatures (M1C1-R4).

TABLE 4: Kinetic Data of CO Oxidation on the M1C1-R4 and M1C1-P4 Catalysts in the Range of 373−423 K

		1st cycle			2nd cycle		
		reaction rate			reaction rate		
catalyst	T (K)	μmol·g$_{cat}^{-1}$·s^{-1}	nmol·m$_{cat}^{-2}$·s^{-1}	sty$_{Mn}$ (s^{-1})	μmol·g$_{cat}^{-1}$·s^{-1}	nmol·m$_{cat}^{-2}$·s^{-1}	sty$_{Mn}$ (s^{-1})
M1C1-R4	373	2.9	18.8	7.6×10^{-4}	3.3	21.4	9.7×10^{-4}
	393	5.9	38.3	1.6×10^{-3}	5.4	35.1	1.4×10^{-3}
	403	6.9	44.8	1.9×10^{-3}	7.6	49.4	2.0×10^{-3}
	413	n.d.	n.d	n.d.	n.d.	n.d.	n.d.
	423	14.2	92.2	3.8×10^{-3}	13.5	87.7	3.6×10^{-3}
M1C1-P4	373						
	393						
	403	0.9	8.9	2.4×10^{-4}	0.8	7.9	2.1×10^{-4}
	413	1.3	12.8	3.4×10^{-4}	1.3	12.9	3.4×10^{-4}
	423	2.0	19.8	5.1×10^{-4}	1.9	18.8	4.9×10^{-4}

ions, and a strong "Mn−O−Ce" interaction account for the marked downward shift and larger H$_2$ consumption recorded by TPR analyses of redox-precipitated catalysts.[5,23,24] Nevertheless, the transient nature of the method, the overlap of surface and bulk processes, and potential H$_2$ spillover phenomena onto ceria carrier,[44−47] altogether hinder a reliable assessment of the surface oxygen mobility and availability from TPR data.[5,23−25,48] Then we probed the "reactive surface oxygen availability" (RSOA) of the representative M1C1-R4 and M1C1-P4 catalysts using CO as reductant.[48] Figure 7 shows the CO oxidation pattern in the range of 293−423 K, while the RSOA values at 323, 373, and 423 K per weight and surface area unit are summarized in Table 3. The M1C1-R4 catalyst features an onset CO oxidation temperature close to room temperature and reaction rates rising until the value of 0.65 μmol·g$_{cat}^{-1}$·s^{-1} at 423 K. Meanwhile, in the range of 323−423 K the RSOA rises from 4 to 200 μmol$_{O_2}$·g$_{cat}^{-1}$, the last corresponding to a minor fraction (<3.5%) of the catalyst oxygen content. A low energetic barrier (ΔH^*, 43 ± 4 kJ/mol) to the oxygen release (Figure 8) confirms that the process is mostly confined to the surface, without any significant contribution of solid-state oxygen diffusion. Constant reaction rates, RSOA, and ΔH^* values throughout the redox cycles are also diagnostic of an excellent stability. The M1C1-P4 system exhibits a considerably weaker oxidative performance, probed by a higher onset oxidation temperature (≈330 K) and lower reaction rates, resulting in RSOA values rising from 0.01 (323 K) to ca. 100 μmol$_{O_2}$·g$_{cat}^{-1}$ (423 K). Although the latter figure corresponds to a fraction

lower than 2% of the total oxygen availability, its steeper dependence on temperature (Figure 8) signals a much higher energetic barrier (ΔH^*, 62 ± 3 kJ/mol) to surface oxygen abstraction. Despite the progressive decay of the CO oxidation rate and RSOA in the second and third cycles, unchanged ΔH^* values (Figure 8) indicate that the surface redox cycle involves the same (e.g., Mn^{4+}) active sites.[15] This different redox behavior relies also on the structural features of the two systems, since superior accessibility of active phase and the strong interaction with ceria promote the electron transfer from O to Mn ions (e.g., O^{2-}−Mn^{4+} → O$^-$−Mn^{3+}), allowing the massive production of *electrophilic* oxygen species oxidizing CO.[48−50] Hard reducibility and low dispersion of crystalline MnO$_x$ phases hinder the RSOA conferring also a poor stability to the coprecipitated system.

An XRD study of the M1C1-R4 (Figure 9A) and M1C1-P4 (Figure 9B) catalysts subjected to reduction treatments at 423 (a), 585 (b), and 720 K (c) has been carried out to address the origin of the different stability. The first is the final temperature of RSOA measurements, while the second and third ones correspond to the first peak maximum (T_{M1}) and final MnO$_x$ reduction in TPR measurements, respectively.[5,23,24] In agreement with Raman data, the XRD of the calcined redox-precipitated system discloses a substantially amorphous pattern (Figure 9A) while both cerianite and pyrolusite (i.e., MnO$_2$) crystalline phases are detected on the coprecipitated one (Figure 9B).[5,23,24] In both cases the reduction at 423 K (curves a) does not yield any detectable structural change, while the XRD patterns of samples reduced at 585 K show different phase transformations.

Besides very small lines for cerianite, the diffractogram of the M1C1-R4 sample (Figure 9A,b) displays poorly resolved peaks at 34.9 and 40.6°, that are typical of the cubic MnO species (JCPDS 7 230). The M1C1-P4 system shows the reflections of the Mn_2O_3 phase (18°, 36.2°, and 37.6°), while those of MnO_2 (37.3° and 45.8°) are no longer visible. These data substantiate the fact that the first TPR maximum of the M1C1-R4 system monitors the straight reduction of "isolated" Mn^{4+} ions to MnO, while for the M1C1-P4 one it is mostly related to the stepwise reduction of the crystalline MnO_2 phase to Mn_2O_3.[5,23,24] Finally, in concomitance with a complete active phase reduction to MnO,[5,23-25] cerianite and MnO peaks are well-resolved in the patterns (profiles c) of both systems reduced.[5,8-12,16,19-25] Therefore, XRD data indicate that the superior RSOA and stability of the redox-precipitated system rely on a full reversibility of the surface redox cycle(s) involving isolated Mn^{4+} ions ($Mn^{4+} \leftrightarrows Mn^{2+}$). Their strong interaction with the ceria matrix hinders the sintering and the consequent formation of less active crystalline MnO_x species.[15] While, the irreversible reduction of MnO_2 clusters to crystalline Mn_2O_3 species explains the decreasing RSOA of the M1C1-P4 catalyst in terms of progressive loss of active surface MnO_2 sites.[15]

(D) Catalytic Oxidation Pattern and Structure–activity Relationships. CO oxidation activity measurements in the range of 373–423 K were performed to highlight the influence of structural and redox properties on the catalytic performance of the $MnCeO_x$ system. Kinetic data are listed in Table 4 in terms of reaction rate per weight and surface unit and average Mn site time yield (sty_{Mn}, s^{-1}) referred to the Mn loading (Table 1). The M1C1-R4 catalyst exhibits a noticeable activity in the range of 373–423 K with reaction rate values rising from ca. 3 to 15 $\mu mol \cdot g_{cat} \cdot s^{-1}$ that even compare with those of Co_3O_4–CeO_2[49] and Au/CeO_2 catalysts.[51] Much lower rate values (Table 4) support the weaker oxidative activity of the M1C1-P4 catalyst, which depends on the different structure and availability of active sites. In fact, while the specific surface rate and the sty_{Mn} values are much lower than the ca. 2 times lower active phase dispersion (Table 1), the Arrhenius plot (Figure 10A) accounts for E_a values of 35–41 and 53–61 kJ/mol for the M1C1-R4 and M1C1-P4 catalysts, respectively. Similar differences (18–20 kJ/mol) in the E_a of CO oxidation were previously ascribed to high MnO_x dispersion and very effective MnO_x–CeO_2 interaction, enhancing the oxidation strength and stability of CeO_2-promoted MnO_x/SiO_2 catalysts.[15] Further, E_a values very close to ΔH^* of RSOA for both catalysts reveal that the surface oxygen abstraction (*reduction step*, CO + σ-O→CO_2 + σ) is the rate-determining step of the CO oxidation, in comparison to a much faster rate of oxygen incorporation onto reduced sites (oxidation step, σ + $^1/_2O_2$ → σ-O).[50] Reaction orders on CO and O_2 pressure of 0.9 and 0.14 (Figure 10B) substantiate the fact that the total oxidation activity of the $MnCeO_x$ system is driven by the electron-transfers promoting the formation of reactive electrophilic species and, in turn, the oxygen mobility.[50] However, reaction rates more than 1 order of magnitude greater than in absence of gas-phase oxygen signal that the CO oxidation implies the (quasi)simultaneous proceeding of the surface reduction and oxidation steps according to the push–pull redox mechanism.[50]

Conclusions

The effects of preparation method and composition on textural and redox properties of $MnCeO_x$ catalysts have been addressed.

The occurrence of nanosize effects on the physicochemical and catalytic oxidation properties of the redox-precipitation system has been documented.

In particular, the main results of this work can be summarized as follows:

Irrespective of the Mn/Ce ratio, the redox-precipitation route ensures large surface area and pore volume, regular pore size distribution and a *molecular* oxide dispersion.

The *molecular* dispersion enhances the reducibility and the surface oxygen mobility in the range of 323–423 K by promoting the electron transfer from oxygen to Mn ions with the consequent formation of very reactive *electrophilic* oxygen species.

Redox-precipitated catalysts feature superior CO oxidation activity and stability under redox reaction conditions.

References and Notes

(1) Matatov-Meytal, Y. I.; Sheintuch, M. *Ind. Eng. Chem. Res.* **1998**, *37*, 309.

(2) Imamura, S. In *Catalysis by Ceria and Related Materials*; Trovarelli, A., Ed.; Imperial College Press: London, U.K., 2002; Vol. 14, p 431.

(3) Bhargava, S. K.; Tardio, J.; Prasad, J.; Foger, K.; Akolekar, D. B.; Grocott, S. C. *Ind. Eng. Chem. Res.* **2006**, *45*, 1221.

(4) Larachi, F. *Top. Catal.* **2005**, *33*, 109.

(5) Arena, F.; Negro, J.; Parmaliana, A.; Spadaro, L.; Trunfio, G. *Ind. Eng. Chem. Res.* **2007**, *46*, 6724.

(6) Abecassis-Wolfovich, M.; Landau, M. V.; Brenner, A.; Herskowitz, M. *J. Catal.* **2007**, *247*, 201.

(7) Silva, A. M. T.; Marques, R. R. N.; Quinta-Ferreira, R. M. *Appl. Catal., B* **2004**, *47*, 269.

(8) Tang, X.; Li, Y.; Huang, X.; Hu, Y.; Zhu, H.; Wang, J.; Shen, W. *Appl. Catal., B* **2006**, *62*, 265.

(9) Terribile, D.; Trovarelli, A.; de Leitnburg, C.; Primavera, A.; Dolcetti, G. *Catal. Today* **1999**, *47*, 133.

(10) Liu, Y.; Luo, M.; Whei, Z.; Xin, Q.; Ying, P.; Li, C. *Appl. Catal., B* **2001**, *29*, 61.

(11) Gil, A.; Gandía, L. M.; Korili, S. A. *Appl. Catal., A* **2004**, *274*, 229.

(12) Li, W. B.; Chu, W. B.; Zhang, M.; Hua, J. *Catal. Today* **2004**, *93–95*, 205.

(13) Lamaita, L.; Peluso, M. A.; Sambeth, J. E.; Thomas, H. J. *Appl. Catal., B* **2005**, *61*, 114.

(14) Barrio, I.; Legórburu, I.; Montes, M.; Domínguez, M. I.; Centeno, M. A.; Odriozola, J. A. *Catal. Lett.* **2005**, *101*, 151.

(15) Craciun, R. *Catal. Lett.* **1998**, *55*, 25.

(16) Imamura, S.; Shono, M.; Okamoto, N.; Hamada, A.; Ispida, S. *Appl. Catal., A* **1996**, *142*, 279.

(17) Qi, G.; Yang, R. T. *J. Catal.* **2003**, *217*, 434.

(18) Adachi, G.-Y. ; Masui, T. In *Catalysis by Ceria and Related Materials*; Trovarelli, A., Ed.; Imperial College Press: London, U.K., 2002; Vol. 3, p 51.

(19) Chen, H.; Sayari, A.; Adnot, A.; Larachi, F. *Appl. Catal., B* **2001**, *32*, 195.

(20) Hamoudi, S.; Larachi, F.; Sayari, A. *J. Catal.* **1998**, *177*, 247.

(21) Hussain, S. T.; Sayari, A.; Larachi, F. *Appl. Catal., B* **2001**, *34*, 1.

(22) Arena, F.; Parmaliana, A.; Trunfio, G. *Stud. Surf. Sci. Catal.* **2007**, *172*, 489.

(23) Arena, F.; Trunfio, G.; Negro, J.; Fazio, B.; Spadaro, L. *Chem. Mater.* **2007**, *19*, 2269.

(24) Arena, F.; Trunfio, G.; Negro, J.; Spadaro, L. *Mater. Res. Bull.* **2008**, *43*, 539.

(25) Arena, F.; Trunfio, G.; Negro, J.; Spadaro, L. *Appl. Catal., B* **2008**, *85*, 40.

(26) Abecassis-Wolfovich, M.; Jothiramalingam, R.; Landau, M. V.; Herrskowitz, M.; Viswanathan, B.; Varadarajan, T. K. *Appl. Catal., B* **2005**, *59*, 91.

(27) Burda, C.; Chen, X. B.; Narayanan, R.; El-Sayed, M. *Chem. Rev.* **2005**, *105*, 1025.

(28) Liang, S.; Teng, F.; Bulgan, G.; Zong, R.; Zhu, Y. *J. Phys. Chem. C* **2008**, *112*, 5307.

(29) Blanco, G.; Cauqui, M. A.; Delgado, J. J.; Galtayries, A.; Perez-Omil, J. A.; Rodriguez-Izquierdo, J. M. *Surf. Interface Anal.* **2004**, *36*, 752.

(30) Wang, Z. L.; Feng, X. *J. Phys. Chem. B* **2003**, *107*, 12563.

Nanostructured MnCeO$_x$ Catalysts

J. Phys. Chem. C, Vol. 113, No. 7, 2009 **2829**

(31) Bumajad, A.; Zaki, M. I.; Eastoe, J.; Pasupulety, L. *Langmuir* **2004**, *20*, 11223.

(32) McBride, J. R.; Hass, K. C.; Poindexter, B. D.; Weber, W. H. *J. Appl. Phys.* **1994**, *76*, 2435.

(33) Buciuman, F.; Patcas, F.; Craciun, R.; Zahn, D. R. T. *Phys. Chem. Chem. Phys.* **1999**, *1*, 185.

(34) Bernard, M. C.; Hugot-Le Goff, A.; Vu Thi, B.; de Torresi, S. C. *J. Electrochem. Soc.* **1993**, *140*, 3065.

(35) Julien, C.; Massot, M.; Rangan, S.; Lemal, M.; Guyomard, D. *J. Raman Spectrosc.* **2002**, *33*, 223.

(36) Romeo, M.; Bak, K.; El Fallah, J.; le Normand, F.; Hilaire, L. *Surf. Interface Anal.* **1993**, *20*, 508.

(37) Larachi, F.; Pierre, J.; Adnot, A.; Bernis, A. *Appl. Surf. Sci.* **2002**, *195*, 236.

(38) Mullins, D. R.; Overbury, S. H.; Huntley, D. R. *Surf. Sci.* **1998**, *409*, 307.

(39) Shyu, J. Z.; Weber, W. H.; Gandhi, H. S. *J. Phys. Chem.* **1998**, *92*, 4964.

(40) Moulder, J. F.; Stickle, W. F.; Sobol, P. E.; Bomben, K. D. In *Handbook of X-ray Photoelectron Spectroscopy*; Physical Electronics Inc.: Eden Prairie, MN, 1995.

(41) Carter, J. C.; Schweitzer, G. K.; Carlson, T. A. *J. Chem. Phys.* **1972**, *57*, 980.

(42) Oku, M.; Hirokawa, K.; Ikeda, S. *J. Electron Spectrosc.* **1975**, *7*, 465.

(43) Wagner, C. D. In *Practical Surface Analysis*, 2nd ed.; Briggs, D., Seah, M. P., Eds.; J. Wiley & Sons, Inc.: New York, 1990.

(44) Wagner, C. D.; Riggs, N. M.; Davis, L. E.; Moulder, J. J. In *Handbook of X-ray Photoelectron Spectroscopy*; Mullenberg, G. E., Ed.; Perkin-Elmer Corp.: Eden Prairie, MN, 1979.

(45) Adem, E. In *VG Scientific XPS Handbook*; VG Scientific Ltd.: The Birches Industrial Estate, West Sussex, 1991.

(46) Zaki, M. I.; Kappenstein, C. *Z. Phys. Chem.* **1992**, *176*, 97.

(47) Bera, P.; Gaten, A.; Hegdé, M. S.; Spadaro, L.; Frusteri, F.; Arena, F. *J. Phys. Chem. B* **2003**, *107*, 6122.

(48) Duprez, D.; Descorme, C. In *Catalysis by Ceria and Related Materials*; Trovarelli, A., Ed.; Imperial College Press: London, U.K., 2002; Vol. 7, p 243.

(49) Luo, J.-Y.; Meng, M.; Li, X.; Li, X.-G.; Zha, Y.-Q.; Hu, T.-D.; Xie, Y.-N.; Zhang, J. *J. Catal.* **2008**, *254*, 310.

(50) Bielañski, A.; Haber, J. In *Oxygen in Catalysis*; Marcel Dekker, Inc.: New York, 1991.

(51) Arena, F.; Famulari, P.; Trunfio, G.; Bonura, G.; Frusteri, F.; Spadaro, L. *Appl. Catal., B* **2006**, *66*, 81.